A time-of-flight correction procedure for fast-timing data of recoils with varying implantation positions at a spectrometer focal plane

M.J. Mallaburn [a],[*], B.S. Nara Singh [a], D.M. Cullen [a], D. Hodge [a], M.J. Taylor [a], M.M. Giles [a], L. Barber [a], C.R. Niţă [b], R.E. Mihai [b], C. Mihai [b], R. Mărginean [b], N. Mărginean [b], C.R. Nobs [c], E.R. Gamba [c], A.M. Bruce [c], C. Scholey [d], P. Rahkila [d], P.T. Greenlees [d], H. Badran [d], T. Grahn [d], O. Neuvonen [d], K. Auranen [d], F. Bisso [d], D.M. Cox [d], A. Herzáň [d], R. Julin [d], J. Konki [d], A.K. Lightfoot [d], J. Pakarinen [d], P. Papadakis [d], J. Partanen [d], M. Sandzelius [d], J. Sarén [d], J. Sorri [d], S. Stolze [d], J. Uusitalo [d], P.H. Regan [e], Zs. Podolyák [e], S. Lalkovski [e], J.F. Smith [f], M. Smolen [f]

[a] *School of Physics & Astronomy, Schuster Building, The University of Manchester, Manchester, M13 9PL, United Kingdom*
[b] *Horia Hulubei National Institute of Physics and Nuclear Engineering, Bucharest, RO 077125, Romania*
[c] *School of Computing, Engineering and Mathematics, University of Brighton, Brighton, BN2 4GJ, United Kingdom*
[d] *University of Jyvaskyla, Department of Physics, P.O. Box 35, FI 40014, Finland*
[e] *Faculty of Engineering and Physical Sciences, Department of Physics, University of Surrey, Guildford, GU2 7XH, United Kingdom*
[f] *School of Engineering and Computing, University of the West of Scotland, Paisley, PA1 2BE, United Kingdom*

ARTICLE INFO

ABSTRACT

Fast-timing measurements at the focal plane of a separator can suffer from poor timing resolution. This is due to the variations in time-of-flight (ToF) for photons travelling to a given detector, which arise from the changes in the implantation positions of the recoil nuclei emitting the γ rays of interest. In order to minimise these effects on timing measurements, a procedure is presented that improves fast-timing data by performing ToF corrections on an event-by-event basis. This method was used to correct data collected with an array of eight LaBr$_3$ detectors, which detected γ rays from spatially distributed ^{138}Gd recoil-implants at the focal plane of the Recoil-Ion-Transport-Unit (RITU) spectrometer. The Generalised Centroid Difference (GCD) method was used to extract a lifetime from data in conjunction with a new procedure to calibrate the time walk. The lifetime of the first 2^+ state in ^{138}Gd, populated by the decay of the $K^\pi = 8^-$ isomeric state, was measured to be 229(24) ps using the ToF-corrected data, which is consistent within three standard deviations to the literature value. The results together with Monte-Carlo simulations show that the ToF correction procedure reduced the uncertainty in the measured lifetimes by 3 % in the case of the spatially distributed nuclei at the focal plane of RITU. However, ~12 % has been estimated for a similar experiment when using a larger focal plane i.e. the Super-FRS at the FAIR facility.
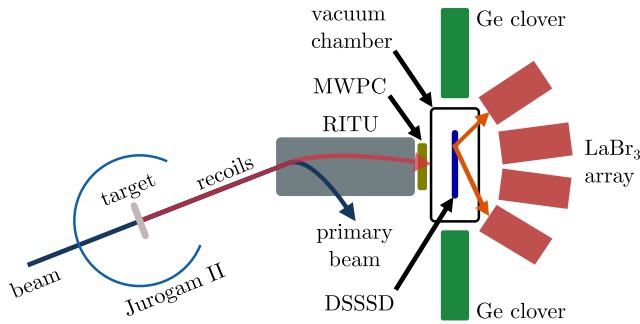
1. Motivation

The lifetime of a nuclear level is a sensitive observable, which is often used to investigate structural features of the nuclear force. These include phenomena such as changes in conventional shell gaps [1], shape coexistence [2], isospin symmetry breaking [3], clustering [4] and particle tunnelling [5–8] in nuclei. In these studies, lifetime measurements have been used to evaluate the roles of different components of the underlying effective nucleon–nucleon interactions (effNNI) used in calculations [3,9,10]. Nuclei at the extremes of nuclear existence will soon become available at a few premier facilities around the world. Lifetimes of excited states in these exotic nuclei are expected

to be particularly sensitive to specific components of the effNNI. However, the state-of-the-art production procedures and low-rates demand optimisation of the experimental techniques used to perform precise lifetime measurements.

Lifetimes of nuclear states are typically observed to be in the range extending from 10^{-15} s and longer. The specific method used to populate the nuclear level of interest and the expected lifetime imposes constraints on the applicability of the available measurement techniques [11–14]. Of these techniques, both the Fast-Timing Method (FTM) and the Recoil Distance Method (RDM) can be employed to measure lifetimes in the range of 10^{-11} s to 10^{-9} s. In the FTM, timing signals corresponding to the γ rays populating and depopulating a level

---

Fig. 1. (left) A schematic top-view illustration of the experimental setup. The orange arrows between the Double-Sided Silicon Strip Detector (DSSSD) and two of the LaBr$_3$ detectors, show that the flight paths for photons can be different as they can originate from nuclei implanted over a large area. (right) Photograph of the eight-LaBr$_3$ detector array together with the three clover detectors of GREAT. The identification numbers used in the text are also indicated. (For interpretation of the references to colour in this figure legend, the reader is referred to the web version of this article.)

of interest are used to measure its lifetime [12]. As the FTM has no requirement on the velocity, v, of the nuclei under study, it can be employed for online measurements both at the target position ($|v| > 0$) and at the focal plane of a separator ($|v| = 0$). In addition, it can also be employed for off-line measurements of nuclear levels populated by the decays of long-lived nuclear states. This is in contrast with the RDM, which requires the detection of γ rays emitted from nuclei with two different velocity regimes at the target position [5–8,15,16]. When using the RDM without any γ-ray coincidence condition, there is the possibility of unobserved γ rays populating nuclear states (side-feeding) that can introduce systematic error into lifetime measurements [13]. This systematic error can be avoided by using coincidentally observed γ rays which reduces the probability of side-feeding by ensuring a γ ray is observed that is known to populate the nuclear state. As the FTM requires at least two γ rays to be observed to calculate a time difference, side-feeding is not an issue.

By positioning the LaBr$_3$ detectors at the focal plane of a separator, the fast-timing technique can be used to measure lifetimes of short-lived states that are populated by β-decaying nuclei or by delayed γ decays of longer-lived isomeric states [17]. In this paper, the FTM was employed at the Recoil-Ion-Transport-Unit (RITU) focal plane in conjunction with the Recoil-Isomer-Tagging (RIT) technique [18–26], which utilises implanted recoils in an isomeric state. Such experiments benefit from a low background environment associated with recoil selection, and therefore can permit measurements of nuclear levels produced with small cross-sections (~1 μb). However, the achievable precision in focal-plane measurements can be affected by the spatial distributions of nuclei of interest. Sources of γ rays, in which the FTM is used in conjunction with a detector array at the target position of a focal plane spectrometer, often do not have large spatial spreads [27,28]. Therefore, the source-to-detector distance remains constant throughout an experimental measurement for each detector used. In the case of measurements at the RITU focal plane, typically recoil-implants have spatial distributions of ~120 mm × 40 mm, leading to a variation in implantation position-to-detector distance. Therefore, γ rays emitted by such recoil-implants with varying spatial positions can suffer from varying time-of-flight paths to a given detector. These geometry-dependent differences in the timing signals of γ rays need to be corrected on an event-by-event basis before employing the FTM. In the present work, a ToF correction procedure is implemented in conjunction with the Generalised Centroid Difference (GCD) method and applied to the data collected for spatially-distributed ^{138}Gd recoils.

2. Experimental setup

A fast-timing experiment was performed at the University of Jyväskylä. Fig. 1(left) shows the experimental setup, which consisted of the Jurogam II array of high purity germanium (HPGe) detectors for the observation of γ rays at the target position [29–31], the RITU gas-filled separator [32], and the Gamma-Recoil-Electron-Alpha-Timing (GREAT) spectrometer for the detection of the implantation and decay of recoils [33]. A 190 MeV ^{36}Ar^{8+} beam with an average current of ~50 enA from the K130 cyclotron was used to bombard a ~1.1-mg/cm^2 thick ^{106}Cd target at the centre of Jurogam II for five days. ^{138}Gd nuclei were thus produced by means of fusion-evaporation reactions, via the 2p2n exit channel. RITU separated the reaction products from the beam and transported them to the focal plane. A Multi-Wire Proportional Counter (MWPC) was positioned at the entrance of GREAT in order to measure the energy loss for the reaction products. The recoiling nuclei were implanted into two side-by-side 60 mm × 40 mm Double-Sided Silicon Strip Detectors (DSSSD). The time-of-flight for recoils passing through RITU was determined from the MWPC and DSSSD detectors. Energy signals in each of the vertically-oriented (x) and horizontally-oriented (y) DSSSD strips were analysed. If the energy deposited in a given 1 mm × 1 mm pixel was found to be in the range expected for the reaction products, the pixel co-ordinates were used to provide the implantation position or the origin of a γ ray. Three HPGe clover detectors were placed surrounding the DSSSD to provide information on the focal-plane γ rays. One of the HPGe clover detectors was positioned above the DSSSD and the other two as shown in Fig. 1 (left). In addition to the standard experimental configuration at the focal plane, eight LaBr$_3$ detectors of 1.5 inch diameter and 2 inch length were placed downstream of GREAT to measure energies and the associated timing of γ-ray transitions following the decay of isomeric states in recoil nuclei implanted into the DSSSD. Each of the LaBr$_3$ detectors was surrounded by 5 mm thick cylindrical lead shielding to reduce the probability of detecting γ rays that scattered in a nearby detector. Fig. 1(right) shows a photograph of the clover and LaBr$_3$ detectors along with the numbering system used to identify individual detectors in the present work. GREAT is usually operated with a planar detector positioned downstream of the DSSSD, i.e. between the DSSSD and where the LaBr$_3$ detectors were placed in the present work. Simulations showed a factor of five increase in the efficiency of the LaBr$_3$ array for the detection of a 200 keV γ ray when the planar detector was not present [34]. The planar detector was therefore removed in the present work to minimise the attenuation of low-energy (<500 keV) γ rays emitted from the recoils implanted into the DSSSD.

The beam current was limited by the requirement that the time between any consecutive recoil-implants detected in the DSSSD should be much longer than the half-life ($T_{1/2}$) of the isomeric state in ^{138}Gd of ~6 μs [35]. During the experiment, the observed implantation rate was ~6 kHz, therefore the average time between any two recoils arriving at any of the pixels of the DSSSD was ~170 μs. Consequently, the implantation positions could be reliably determined, enabling the ToF corrections to be performed.

The LaBr$_3$ detectors were coupled to fast R9779 photomultiplier tubes (PMT), having two outputs: anode and last dynode [36]. The dynode signal was processed using Ortec 474 timing filter amplifiers [37] in order to obtain the energy of a γ ray. The signal from the anode was processed to obtain timing information of the γ ray through an Ortec 935 constant fraction discriminator (CFD) [38] and an Ortec 566 Time-to-Amplitude Converter (TAC) [39]. Seven TACs were used to record information from the 28 unique detector pairs using a multiplexed stop circuit [12]. Lyrtech Analogue-to-Digital Converter (ADC) cards were used to digitise signals recorded using the Total Data Readout method and a 100-MHz clock [40]. Utilising the GRAIN software package [41], the γ-γ coincidence data were sorted into three dimensional E_i-E_j-TAC$_{ij}$ histograms, containing energy signals from detectors i and j and TAC signal started with a timing signal from the CFD connected to detector i and stopped with that connected to detector j. Sorted data were subsequently exported from GRAIN and analysed using the RADWARE software suite [42] and kmpfit [43]. Kmpfit uses a least-squares minimisation procedure based on the Levenberg–Marquardt algorithm [44,45].

3. Timing measurements and calibration

An analysis of data from fast-timing measurements with spatially distributed sources involves the minimisation of any errors originating from the positioning and size of the detectors in the experimental setup as well as the processing of detector signals. In the case of a spatially distributed source, the path length between a γ-ray emission point and any given detector can vary between measurements. This leads to differences in the flight paths of γ rays, resulting in a variation of the timing of each γ ray with the position of its emission point. Therefore, it was necessary to correct the recorded time values (TAC$_{ij}$) for differences in time-of-flight for photons producing the start and stop timing signals. This correction is subsequently referred to as the ToF correction. The time of the output signal from a CFD is known to vary as a function of incident γ-ray energy. This systematic variation is known as the time walk [46,47]. The procedures used to correct for both ToF differences and time walk are detailed in the following sub-sections.

3.1. Energy and time resolutions of the LaBr$_3$ array

To measure the energy and time resolution of the LaBr$_3$-detector system, a ^{60}Co source was placed at the centre of the array on the exterior of the vacuum chamber and data were recorded. The FWHM of the peak corresponding to the 1333 keV transition in the ^{60}Co-source decay was found to be 49 keV in the summed-energy spectrum of all eight LaBr$_3$ detectors. The intrinsic photo-peak efficiency for this γ ray was measured to be 12.2(14) %. The timing resolution of the detector system was measured using the 1173 keV γ ray emission from the decay of ^{60}Co as a start signal to the TACs and the 1333 keV γ ray as the stop signal. These γ rays (de)populate the 2^+ state in ^{60}Ni, which has a known half-life of 910(20) fs [48]. As the two γ rays are emitted within a time period that is much shorter than the timing resolution of the detector pair, the corresponding time spectrum is expected to approximate a Gaussian distribution and the observed standard deviation gives the time resolution. Therefore, 3D-histograms (E_i, E_j, TAC$_{ij}$) were made using the ^{60}Co source data set with a time coincidence window of 30 ns between γ rays. TAC$_{ij}$ values were then projected by placing energy gates according to the observed γ-ray energies and
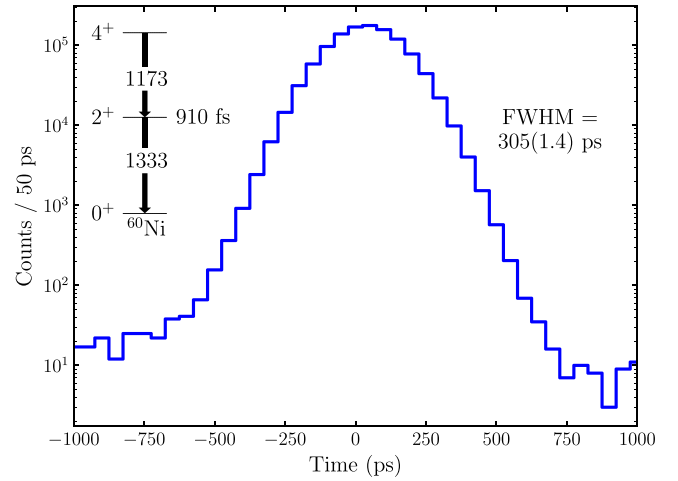

Fig. 2. A sum histogram of the timing response of all the 28 LaBr$_3$ detector pairs in the array. The events correspond to the time difference of the γ rays populating and depopulating the 2^+ state with a half-life of 910(20) fs in ^{60}Ni, the daughter product of ^{60}Co. The corresponding TACs were started with the timing signal of the 1173 keV transition and stopped with that of the 1333 keV transition.

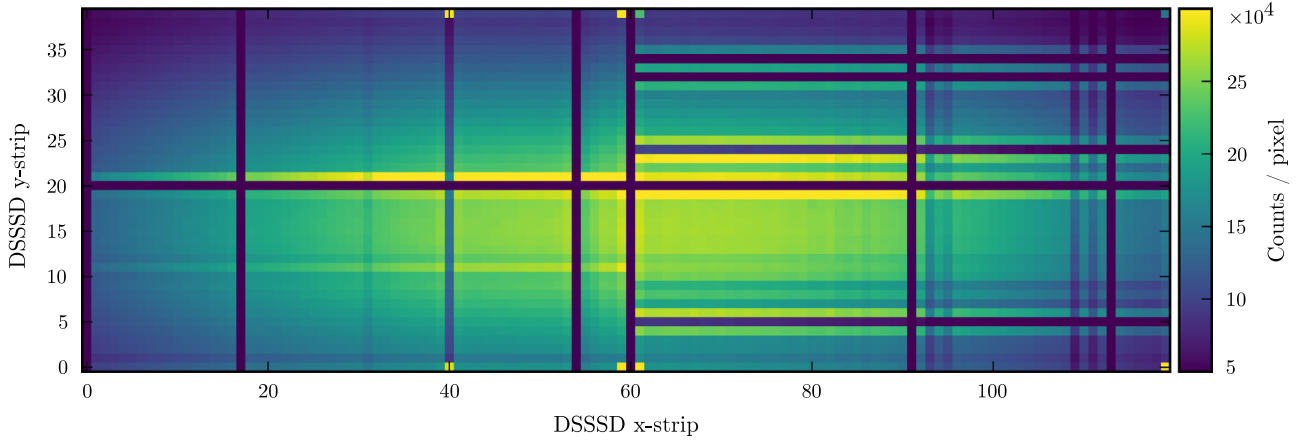energy resolutions for 1173 keV (E_i) and 1333 keV (E_j). The centroids of the TAC$_{ij}$ values were calculated for each detector combination and subtracted from each recorded time value in a subsequent re-sorting of the data. This ensured that the time spectrum for each detector pair was synchronised to a common prompt time value of 0 ps. Fig. 2 shows the summed time spectrum from which a FWHM of 305(1.4) ps (σ ~127 ps) was obtained. The observed individual FWHM values for the time spectra of the 28 unique detector-pairs ranged from 264.0(9) ps to 413.1(12) ps.

For the measurement of the lifetime of the 2^+ state in ^{138}Gd [35], the timing of 221 keV and 384 keV γ rays were required. At such relatively small energies, time resolutions are known to be worse than that obtained for γ rays with energies of 1173 keV and 1333 keV due to an increase in CFD time jitter [12,49]. For example, a similar procedure was used to calculate the timing resolution of the detection system using the 340 keV and 245 keV γ rays, emitted during the decay of a ^{152}Eu source. The result was a FWHM of ~570 ps (σ ~240 ps), which better represents the expected resolution for the ^{138}Gd γ rays used in the present work.

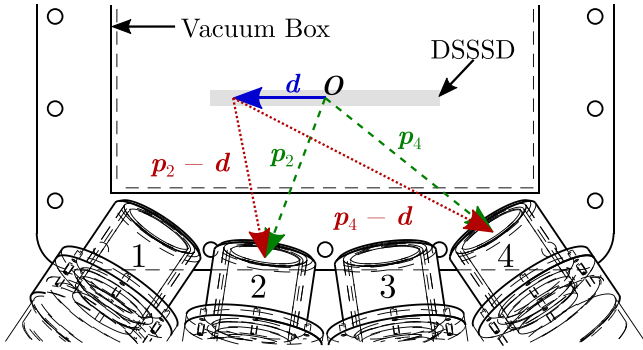### 3.2. ToF correction

Fig. 3 shows the DSSSD pixel map of the implanted recoil nuclei from the present data. The RITU magnet settings were adjusted so as to distribute the recoil implants as homogeneously as possible over all of the pixels, minimising the implantation rate per pixel. Fig. 4 shows the arrangement of LaBr$_3$ detectors, which were positioned approximately 100 mm from the centre of the DSSSD. Therefore, the implant-to-detector distances were comparable to the total length (120 mm) and width (40 mm) of the DSSSD in this setup. With the specific geometry of the present experiment, it can be shown (cf. Section 5) that the flight path for photons varied from ~90 mm to ~185 mm, resulting in the ToF differences as large as ~330 ps for recoils distributed across the DSSSD as shown in Fig. 4.

The distances between any given DSSSD pixel and any two of the LaBr$_3$ detectors can be calculated by taking the centre of the DSSSD as the origin O of a coordinate system and using vector addition. An example is shown in Fig. 4 for the case where Detectors 2 and 4 provide the TAC-start and -stop signals, respectively. The difference in time-of-flights, Δt_{pos}, between photons arriving at the start detector (2) and

Fig. 3. Variation of implantations of recoils per pixel over the area of the two side-by-side DSSSDs in the present work. The x- and y-axes give x- and y-strip numbers, respectively. The coloured-axis gives the number of implantations for a given (x,y) pixel. The dark lines correspond to the strips that were not useable due to the presence of high electronic noise. (For interpretation of the references to colour in this figure legend, the reader is referred to the web version of this article.)

Fig. 4. A top-view representation of the fast-timing setup with the LaBr$_3$ detectors at the focal plane of RITU. Photons emitted from a given DSSSD pixel position have different flight times to each of the detectors used to measure the timing (in this example detectors 2 and 4). This is illustrated by the difference in magnitude of the dotted line (red) vectors. The solid (blue) vector shows the position of a pixel, whilst the dashed (green) vectors show the positions of the two LaBr$_3$ detectors relative to the centre of the DSSSD. A resultant time offset is calculated as described in the text. The DSSSD is shown (not to scale) as a rectangle for illustration purposes.

the stop detector (4), each emitted from a DSSSD pixel with a position vector $\boldsymbol{d}$, is given by

$$\Delta t_{\text{pos}} = \frac{|\boldsymbol{p}_2 - \boldsymbol{d}| - |\boldsymbol{p}_4 - \boldsymbol{d}|}{c},\qquad (1)$$

where $\boldsymbol{p}_{2(4)}$ denotes the position vector of Detector 2(4) and c is the speed of light. This can be visualised as the difference in magnitudes of the dotted line (red) vectors shown in Fig. 4.

Fig. 5 demonstrates the effect of the Δt_{pos} correction on the timing of the 779 keV (3$^-$-state decay) and 344 keV (2$^+$-state decay) γ rays from a ^{152}Eu source. In order to obtain a large value for Δt_{pos}, the source was intentionally placed at two positions close to the two extreme edges of the exterior of the GREAT chamber (see the inset on the left of Fig. 5 (b)). The output from Detectors 1 and 8 served as the start and stop signals for the TAC, respectively. The half-life of the 4$^+$ state in ^{152}Gd is known to be 32.0(27) ps [50], which is small compared to the intrinsic time resolution ($\sigma \sim$127 ps) of the LaBr$_3$-detector system used in the present work. Therefore, the corresponding timing distribution is expected to be approximately Gaussian. The time spectrum shown in blue (thick line) in Fig. 5(a) was collected with the source positioned at the bottom-left of the exterior of the GREAT vacuum chamber when viewed looking upstream of the recoil axis. The paths of photons for this source position are shown in blue (thick line) in the left inset of Fig. 5(b). The time spectrum shown in red (thin line) was collected by placing the source at the bottom-right of the vacuum chamber. The centroids of the two peaks in these two time spectra differ by 1017(8)

ps. Fig. 5(b) shows the same data as in Fig. 5(a), but with Δt_{pos}, i.e. the ToF difference given by Eq. (1), added to the recorded TAC$_{18}$ value for the LaBr$_3$-detector-pair (1, 8) on an event-by-event basis. The difference in the centroids of the two spectra shown in Fig. 5(b) was reduced to 2(10) ps, which is consistent with zero. The increased error, compared to that for the uncorrected centroid difference, is due to the uncertainty contributions (6 ps for this detector-pair) from the detector and source positions. When considering multiple detector-pair combinations, discounting only those combinations with low statistics, the mean uncertainty was found to be ±3.3 ps. It is noted that the mean value of the ToF-corrected centroid differences was 3(4) ps, suggesting no significant systematic error was introduced by the ToF correction. Despite being consistent within experimental uncertainty, one possibility for the corrected centroid difference having a non-zero value is that the timing of the detector signal may exhibit a dependence on the incident γ-ray angle. In the present work, any such effect was less than the observed statistical deviation in the timing. As such, the position uncertainty is not included for the analysis performed in Section 4.

This analysis, using data collected with a source placed at two extreme positions, highlights the need for the ToF correction for the measurements using spatially separated sources. It should be mentioned that during an experiment, the nuclei emitting γ rays of interest are distributed over the DSSSD (cf. Fig. 3), but not generally on the exterior of the vacuum chamber. If uncorrected, a broadened time distribution would be observed that would result in a lower uncertainty on the centroid, thus affecting the accuracy of the lifetime determination. The ToF correction for this more realistic situation is discussed in detail in Section 5.

3.3. Walk correction

The CFD timing signals have a mean value, or centroid, that varies as a function of γ-ray energy. This is known as the time-walk [46,47]. The centroid, C, of a time (t) distribution, $D(t)$, is defined as

$$C = \frac{\int_{t_{\text{min}}}^{t_{\text{max}}} t\, D(t)\, \mathrm{d}t}{\int_{t_{\text{min}}}^{t_{\text{max}}} t\,\mathrm{d}t},\qquad (2)$$

where t_{min} and t_{max} are the limits that bound t, chosen experimentally as the points where $D(t)$ becomes indistinguishable from background. The time distribution of two γ rays (de)populating a nuclear state with a lifetime much smaller than is measurable, given the resolution of the detection system, is known as the prompt response function (PRF). The PRF depends on the energies of the observed γ rays and thus, the centroid of the PRF distribution is also function of the γ-ray energies. The prompt response difference (PRD) is calculated by taking
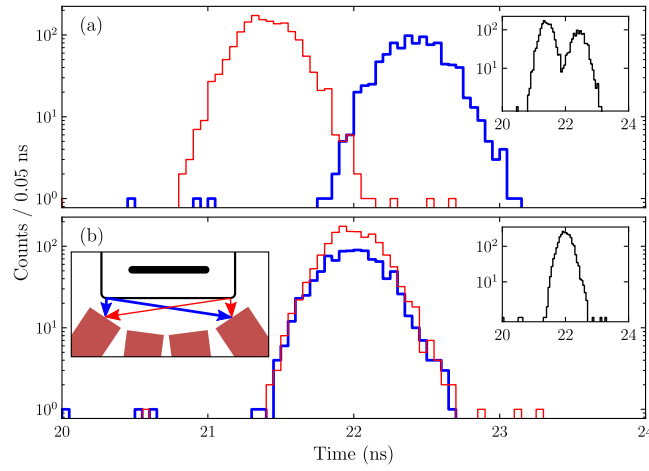
Fig. 5. Time spectra for the 779 keV and 344 keV γ rays from the decay of ^{152}Eu which were detected in LaBr$_3$ Detectors 1 and 8, highlighting the effect of the source position on Δt_{pos}. The inset on the left of (b) shows the two positions of the source placed on the chamber. The red and blue colour coding of the arrows is used to identify the source positions in this inset with the histograms in the main figure. Data without and with the ToF corrections are shown in (a) and (b), respectively. The intensities of the two peaks are not similar due to different counting times and solid angles at the two source positions. The black histograms in the insets on the right present the sum of the two (red and blue) histograms in the main panels. (For interpretation of the references to colour in this figure legend, the reader is referred to the web version of this article.)

the difference of two PRF-centroids, C, obtained from the inverting of the start- and stop-signal γ-ray energies, i.e.

$$\text{PRD}(E_1, E_2) = C\left(E_1, E_2\right) - C\left(E_2, E_1\right), \tag{3}$$

where E_1 and E_2 are the γ-ray energies and their order in the brackets denotes the corresponding signal pulses being used to start (first) or stop (second) a TAC. The walk can be corrected by using a source (e.g. ^{152}Eu) to obtain a data set of PRDs for full-energy peak events as a function of γ-ray energy. This energy dependence can be described by the prompt response difference function (PRDF) [12] which has the form,

$$\text{PRDF}(E) = \frac{a}{\sqrt{E + b}} + cE + d, \tag{4}$$

where a, b, c and d are free parameters that are varied to obtain the best fit to the source data. For convenience, these free parameters are subsequently referred to by a single label, $P = [a, b, c, d]$.

In fast-timing measurements, time spectra are constructed for two different γ rays. Therefore, the resulting PRD is constructed as the linear superposition of the walk contribution from each γ ray, i.e.

$$\text{PRD}(E_1, E_2) = \text{PRDF}(E_1) - \text{PRDF}(E_2). \tag{5}$$

A measurement of $\text{PRD}(E_1^s, E_2^s)$ may be made using a calibration source (e.g. ^{152}Eu) which has a precisely known lifetime, τ^s (i.e. with uncertainty of order <1 ps). The superscript s denotes that E_1^s and E_2^s correspond to the populating and depopulating γ rays of a level in a source. The uncertainty in τ^s should be much smaller than the observed timing resolution for LaBr$_3$ detectors (typically >100 ps). The measured $\text{PRD}(E_1^s, E_2^s)$ values can then be obtained from

$$\text{PRD}(E_1^s, E_2^s) = \Delta C^s - 2\tau^s, \tag{6}$$

where

$$\Delta C^s = C_{\text{delayed}}^s - C_{\text{anti-delayed}}^s. \tag{7}$$

C_{delayed}^s is the centroid of the delayed time spectrum and $C_{\text{anti-delayed}}^s$ is the centroid of the anti-delayed time spectrum of the source data as defined in Ref. [12].

The lifetime, τ, of a level under study, which is populated and depopulated by the γ rays with energies of E_1 and E_2, respectively, can then be deduced by using

$$\tau = \frac{\Delta C - \text{PRD}(E_1, E_2)}{2}. \tag{8}$$

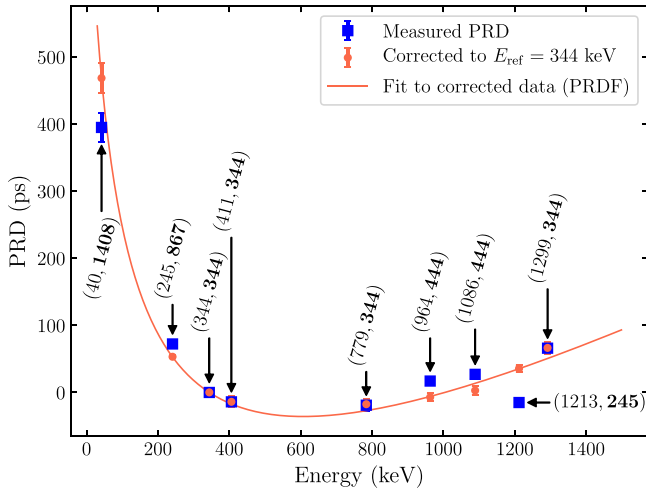In this case, ΔC corresponds to the nuclear level under study [51].

For a given array of LaBr$_3$ detectors, the $\text{PRD}(E_1^s, E_2^s)$ values are obtained for different combinations of γ rays using a calibration source. In the present work, a ^{152}Eu-source was positioned at the centre of the vacuum chamber exterior. The selected γ-ray pairs (E_1^s, E_2^s) (in keV) were; (1086,444), (964,444), (245,867), (1213,245), (1299,344), (779,344), (411,344) and (40,1408). It should be noted that the last pair had an additional condition that a coincident 122 keV γ ray was detected in a focal-plane clover HPGe detector. This condition avoided selection of these γ rays in the energy range chosen for 40 keV due to partial energy detection e.g. from a Compton scatter. In addition, the constraint that $\text{PRD}(E_1^s, E_1^s) = 0$ (cf. Eq. (5)) has been implemented by fixing the point (344, 344) to zero with a small uncertainty. The time spectra were synchronised to a common prompt-event time of 0 ps and summed over each detector pair for a given pair of γ-ray energies in accordance with the GCD method [12]. The PRD was calculated for each of these summed spectra (cf. Eq. (6)). Fig. 6 displays these PRDs as blue squares over a range of energies, E_1^s, with labels showing both E_1^s and E_2^s (bold font). The circular data points were derived using a procedure discussed below.

If one of the energies is fixed to a reference energy E_{ref} then the PRD can be treated as a function of a single energy, allowing more γ-ray pairs to be plotted on the same axes as shown by light red circles in Fig. 6. A reference energy of 344 keV, which corresponds to the 2^+ to 0^+ γ-ray transition in ^{152}Gd, was used in the present analysis (cf. Fig. 6).

By considering Eq. (5), the $\text{PRD}(E_1, E_2)$ for an arbitrary pair of γ ray energies can be calculated from the parameters P. Thus, Eq. (5) describes a surface function in which the E_1-axis shows the average time walk contribution from the start signal. Similarly, the E_2-axis corresponds to the stop-signal time walk. To fit a single line to data points which are distributed across the surface $\text{PRD}(E_1, E_2)$, they are modified such that they have no dependence on one of these axes. Choosing the fixed axis to be the second listed (i.e. E_2 in $\text{PRD}(E_1, E_2)$), the data are therefore modified by the addition of

$$t_m(E_2^s, E_{\text{ref}}) = \text{PRDF}(E_2^s) - \text{PRDF}(E_{\text{ref}}), \tag{9}$$

where E_{ref} is an arbitrary reference energy that need not correspond to the source used. In the present work, however, an E_{ref} of 344 keV was chosen, which does correspond to the source, such that the required modifications to the overall data set was minimised. It can be seen that the addition of $t_m(E_2^s, E_{\text{ref}})$ to the data results in a PRD with no dependence on E_2, but with an introduced dependence on E_{ref}. Therefore, all data acquired with $E_2^s = E_{\text{ref}}$ remain unmodified. This

Fig. 6. A plot of the prompt response difference function, PRDF. The square (blue) points show the prompt response differences (PRDs) obtained using a ^{152}Eu-calibration source. The solid line represents a fit to the data points which were modified to have a reference energy, E_{ref}, of 344 keV, shown by circular data points (light red). The data labels show the relevant plotted energy and reference energy (bold font), respectively, for the measured PRDs. See the text for details. The errors on the data points in some cases are smaller than the symbols with a typical range of ~2 ps to 9 ps. The value at 40 keV has a larger uncertainty due to lower statistics caused by the requirement of an additional HPGe coincidence and the fixed point at 344 keV has an error defined as 10^{-6} ps.
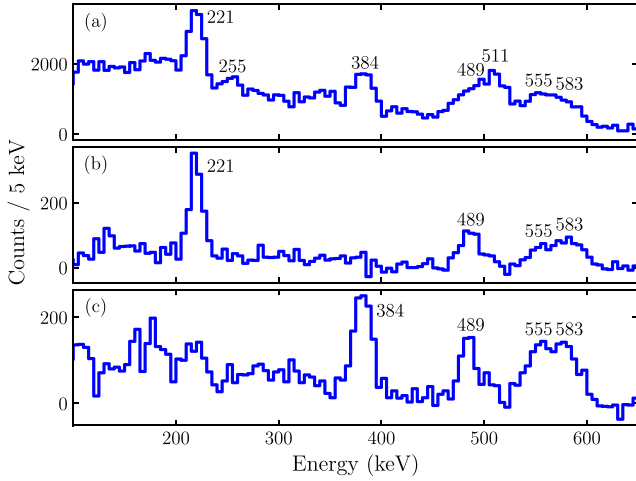
Parameter	Value
a (ps keV$^{\frac{1}{2}}$)	9900(800)
b (keV)	45(10)
c (ps keV^{-1})	0.300(20)
d (ps)	−600(40)

the case of the 4^+ to 2^+ and 2^+ to 0^+ γ-ray transitions in ^{138}Gd (with energies 384 and 221 keV, respectively), the time-walk correction was thus obtained to be −80.6(31) ps. The uncertainty was calculated using the variance–covariance matrix for P, as provided by the least-squares minimisation program, and a software package [52].

It is noted that the fitting procedure for the PRD data presented in this work differs from the currently accepted method [46]. The existing method can be summarised briefly as follows: Firstly, choose measured PRDs that share a common reference energy and obtain a best fit line. Secondly, find a single shift parameter to be added to the data points with a different, but common, reference energy by means of least-squares optimisation. This second step is repeated for as many different reference energies as exist in the measured PRDs. Lastly, with all data modified to the same reference energy, redo the best line fit that was conducted in the first step [46].

The second step in the paragraph above shifts part of the recorded data based on the values of those data used in the first step, and thus the modified data points can no longer be considered to be independent of the unmodified data. This, in turn, makes the subsequent fitting of both modified and unmodified data together difficult without care being taken when implementing a fitting procedure to account for a dependent data set. As the modified data points are shifted in parallel, i.e. the same shift parameter is added to each measurement, another form of correlation is introduced which needs to be accounted for. With the new method in the present work, these correlation issues are avoided as the PRD data are unmodified, i.e. they remain independent measurements. The shift, given by Eq. (9), is defined entirely in terms of the parameters of the walk equation (Eq. (4)) and thus is performed in each iteration of the final fitting procedure until a minimum summed square distance is obtained. This ensures that the change in $\sum_i R_i^2$ between iterations, as a function of each parameter in P, provides a full description, including any correlation effects, of how well the model fits the data. Hence, after conversion of the iterative procedure, a final set of parameters are obtained that best describe the data for the given model. The fitting procedure described in this work reduces the complexity of obtaining the time walk parameters, as there is no need to propagate the uncertainties (and covariances) between an initial set of parameters, the shift parameters, and a final set of parameters. The parameter (co)variances are simply those reported after completion of the iterative procedure.

It is also noted that the existing method [46] promotes the re-use of PRD data, owing to the fact that $\mathrm{PRD}(E_1^s, E_2^s) = -\mathrm{PRD}(E_2^s, E_1^s)$. However, this also introduces a similar dependency issue when a best fit procedure is performed due to half of the data points being exactly negatively correlated with the other half from the same relation. In the present work, whether E_1^s corresponds to a populating or depopulating γ ray is chosen, rather than repeated, for each data point in a way that best distributes the PRD data across the energy range of interest. For example, data were initially labelled such that the first energy corresponded to the populating γ ray of a specific state, and the second energy corresponded to the depopulating γ ray. Some of the data points used in Fig. 6, such as (245, 867), take the opposite convention. In this case, (867, 245) was not used, as it has equal magnitude and opposite sign to the point labelled (245, 867), and is therefore correlated. The choice of (245, 867) over (867, 245) was made because having a point at 245 keV was deemed to be better as nearby points, at 779 and 964 keV, already constrain the PRDF curve in the region of 867 keV.
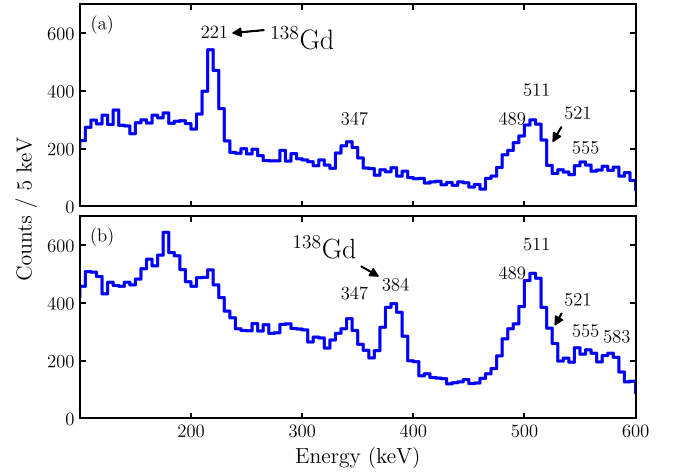
can be seen in Fig. 6 for points where the circular corrected data overlaps the square uncorrected data (e.g. at 344 keV or 411 keV). It is noted a slight shift is observed at 779 keV due to an asymmetric gating condition that favoured the low-energy side of the 344 keV peak, which was imposed to improve the peak-to-background ratio of the selected events. More generally, all data acquired with the same E_2^s are shifted by the same amount (cf. data at 964 and 1086 keV in Fig. 6).

The importance of the transformation described by Eq. (9) is that it is defined entirely by the parameters, P, the stop-signal energy, E_2^s, and an arbitrarily chosen reference energy. This feature allows for the modification to be performed to the data as part of the least squares minimisation procedure used to determine the parameters P. To achieve this, a least squares minimisation program was used [43] that requires the definition of a residuals function. The residuals function, R_i, used was

$$R_i = \frac{\mathrm{PRD}_i + t_m(E_{2i}^s, E_{\mathrm{ref}}) - \mathrm{PRDF}(E_{1i}^s)}{\sigma_i}, \qquad (10)$$

where PRD_i (σ_i) is the measured PRD value (uncertainty) of the ith data point and PRDF is defined in Eq. (4). It is noted that the uncertainties in the energies have been ignored as the error on the PRD values dominated. The least squares minimisation program subsequently minimised the number given by $\sum_i R_i^2$ by means of iterative modification to the parameters P using a modified Levenberg–Marquardt algorithm [43–45]. It is noted that, whilst discussed in the language of a modification to the data, Eq. (10) can also be considered equivalently as the weighted difference between a point, PRD_i, and the surface function described by $\mathrm{PRDF}(E_{1i}^s) - \mathrm{PRDF}(E_{2i}^s) + \mathrm{PRDF}(E_{\mathrm{ref}})$. This last term is arbitrary; defined only to represent the data on a single axis, and may be dropped in favour of performing a fit of the data to the surface function described by Eq. (5) alone.

The procedure described above was applied to the present data, shown as square (blue) points in Fig. 6. The circular (light red) points, calculated by $\mathrm{PRD}_i + t_m(E_{2i}^s, E_{\mathrm{ref}})$, were the final corrected-data values which correspond to a reference energy of 344 keV. The (light red) line is the best estimate for Eq. (4) ($\mathrm{PRDF}(E_1^s)$) given the PRD_i data. Table 1 gives the final converged set of parameter values P and, together with Eq. (5), $\mathrm{PRD}(E_1, E_2)$ can be calculated for any pair of energies. For

Fig. 7. Subtracted energy spectra collected with the LaBr$_3$ array at the focal plane of RITU. The energy projection of the (E_i, E_j, TAC$_{ij}$) 3D histogram with no energy condition (a). The time between recoil implantation and the subsequent detection of a γ ray was used to subtract events from longer-lived states. The energy of γ rays detected in coincidence with 384 keV (b) and 221 keV (c) γ rays from the decay of the 4^+ and 2^+ states in ^{138}Gd, respectively. Both (b) and (c) implement energy-based subtraction in addition to the recoil-decay time subtraction. These spectra were not used in calculation of the lifetime.

Fig. 8. Energy spectra collected with the LaBr$_3$ array at the focal plane of RITU. The energy of γ rays detected in coincidence with 384 keV (a) and 221 keV (b) γ rays from the decay of the 4^+ and 2^+ states in ^{138}Gd, respectively. The peaks labelled as 347 and 521 keV correspond to the decays of the first excited states in ^{138}Sm and ^{138}Nd, respectively, which are part of the ϵ/β^+-decay chain of nuclei originating with ^{138}Gd. The ϵ/β^+-decay peaks are visible as no background subtraction was performed.

Another benefit to the method presented in this work is that a single energy pair can be used with no other pair sharing a common energy, e.g. the point labelled (40, 1408) in Fig. 6. When shifting data onto a curve, at least two points are required as one point would shift exactly onto the curve, adding no additional constraint to the data set. Whilst not explored further in the present work, this consequence allows for greater freedom in the selection of γ-ray pairs using other sources, e.g. ^{60}Co, to obtain more PRD data points.

4. Results

In the present fast-timing measurement, the first 2^+ state in ^{138}Gd [35] was populated by the decay of the corresponding 8^- isomeric state with a half-life of 6.2(2) µs. In-beam data were sorted into a (E_i, E_j, TAC$_{ij}$) 3D-histogram, containing events that were recorded within 18 µs following a recoil implantations into the DSSSD. A 4 ns condition was placed on the time between the observed γ rays to discard those data corresponding to nuclear-state lifetimes much longer than those of interest. It is noted that the TAC$_{ij}$ values were synchronised to a common prompt-event time of 0 ps whilst sorting, allowing the data to be summed in accordance with the GCD method [12]. In a previous experimental work which identified the K$^\pi$ = 8^- isomer in ^{138}Gd using a fusion evaporation reaction, an isomeric yield of $\sim$ 1.4% was estimated [19]. Consequently, a small number of γ rays arising from the isomeric decay at the focal plane were observed. Fig. 7 shows an energy projection of the 3D-histogram which has been background subtracted with events that were detected between 27 µs and 45 µs following a recoil implantation. The result of the subtraction is to remove longer-lived background events that were also present in the relatively short-lived data. It is noted that this background-subtracted data set was not used in the analysis to determine the lifetime of the states. It is only shown to illustrate the quality of these data. Fig. 8 shows the energy projection of the (E_i, E_j, TAC$_{ij}$) 3D histogram with no ToF correction performed when, (a), the start signal was chosen to have an energy of 384 keV and (b), the stop signal was chosen to have an energy of 221 keV. These energies correspond to the $4^+ \rightarrow 2^+$ and $2^+ \rightarrow 0^+$ γ decays in ^{138}Gd, respectively. Fig. 8 also shows peaks at 347 keV and 521 keV corresponding to the γ decay of excited states in ^{138}Sm and ^{138}Nd, respectively. These nuclei were produced as part of

a chain of several ϵ/β^+ decays, starting with the decay of the ^{138}Gd 0^+ ground state [53]. Using these spectra, the peak to background ratios corresponding to the 221 keV and 384 keV γ ray peaks can be determined.

Fig. 9 shows the LaBr$_3$-time spectra for the γ rays populating and depopulating the 2^+ state in ^{138}Gd ((a) and (b)). The events in these histograms were gated by the corresponding $2^+ \rightarrow 0^+$ and $4^+ \rightarrow 2^+$ γ-ray peaks in the energy spectra (cf. Fig. 8) and correlated with recoil-implants within the time window of 18 µs. The spectra on the left (Figs. 9(a), (c) and (e)) and right (Figs. 9(b), (d) and (f)) show data without and with the ToF corrections, respectively. The difference in centroid values, ΔC, between the delayed and anti-delayed [51] time distributions, shown in blue and red lines, respectively, are plotted as (red) squares in (c) through (f). These measured centroid difference values, denoted ΔC_m, are given in Table 2. A reduction in the uncertainty of ΔC_m is expected for the ToF correction to be considered effective. The (black) triangular and (blue) circular data points in (c) and (d) show the centroid difference calculated from time spectra projected from the 3D histogram with the start signal energy selected to correspond to 384 keV as a function of the stop signal energy. The analogous points in ((e) and (f)) show the centroid differences acquired with the stop signal energy selected to be 221 keV as a function of the start signal energy. The solid lines were derived by fitting a linear function to the triangular points that correspond to the time response of the Compton scattered background. Several data points, shown as (blue) circles, were excluded from the background interpolation due to possible contamination of non-Compton scattered (full-energy peak) events. These were considered to be unrepresentative of the background under the peaks of interest, which was expected to consist mainly of Compton scattered γ rays of higher initial energy. In ((c) and (d)), the data point at 260 keV was excluded as it corresponds to a γ ray emitted during the decay of the 2^+ state in ^{136}Sm [54], which was produced alongside the main reactant in the fusion-evaporation reaction. The peak labelled 255 keV in Fig. 7(a) shows the presence of this isotope in this work. The data points at 150 keV and 170 keV were also excluded to avoid systematically biasing the result as both are far from 221 keV and their values were such that the shape of the background response was difficult to determine. In ((e) and (f)), the two points with largest energy (427 keV and 452 keV) were excluded due to a possible overlap with the $4^+ \rightarrow 2^+$ γ ray transition in ^{136}Sm. The two points at 330 keV and 350 keV were excluded due to overlap with the 347

Table 2
Lifetime values, and intermediate parameters, obtained from the data shown in Fig. 9 using the GCD method. The columns labelled as No ToF Correction and ToF-corrected refer to the results without and with ToF corrections, while the ΔC, α and τ rows give the centroid difference between the delayed and anti-delayed time spectra, the peak to background ratio and the lifetime of the nuclear level of interest, respectively. Suffixes m, b, and p denote the measured, interpolated background and inferred full-energy peak centroid difference values, respectively. The Gate row shows which γ ray energy was selected in the data.

	No ToF correction		ToF-corrected	
Gate:	384 keV	221 keV	384 keV	221 keV
ΔC_m (ps)	289(15)		290(15)	
ΔC_b (ps)	223(33)	210(90)	212(33)	230(100)
α	0.85(6)	0.86(6)	0.87(6)	0.86(6)
ΔC_p (ps)	370(50)		380(50)	
τ (ps)	225(25)		229(24)	

keV γ ray of ^{138}Sm, as shown in Fig. 8. The dashed lines show the one-standard-deviation intervals above and below the fitted lines and the (red) crosses mark the interpolated values at which the background timing was inferred. These interpolated background-centroid difference values, denoted ΔC_b, are given in Table 2.

The contribution to the measured centroid difference due to the full-energy peak events, ΔC_p, shown in Table 2, was calculated using the equation,

$$\Delta C_p = \Delta C_m + \frac{1}{V_{tc(384)}^{-1} + V_{tc(221)}^{-1}} \left[\frac{tc_{(384)}}{V_{tc(384)}} + \frac{tc_{(221)}}{V_{tc(221)}} \right],$$

where $tc_{(i)} = \dfrac{\Delta C_m - \Delta C_{b(i)}}{\alpha_{(i)}}$, (11)

and $V_{tc(i)} = \dfrac{V_{\Delta Cm}}{\alpha_{(i)}^2} + \dfrac{V_{\Delta Cb(i)}}{\alpha_{(i)}^2} + \dfrac{V_{\alpha(i)} \left(\Delta C_m - \Delta C_{b(i)} \right)^2}{\alpha_{(i)}^4}.$

where α is the full-energy peak to background ratio, calculated from the energy projections of the 3D histograms (cf. Fig. 8) by interpolation of a linear background under the peaks of interest. A suffix of either $i = 384$ or $i = 221$ denotes the gate used as specified in Table 2 [55] and V is used to denote the variance on the parameter in its suffix. It is noted that Eq. (11) differs from that given in Ref. [55] by taking the weighted mean of the correction terms (tc) instead of the standard mean. This was required in the present work due to the significant difference in precision on the centroid difference of the background interpolated under each peak. The variance on ΔC_p, to first order, was therefore

$$V_{\Delta Cp} = \left(V_{tc(384)}^{-1} + V_{tc(221)}^{-1} \right)^{-2} \left(\left[V_{tc(384)}^{-1} + V_{tc(221)}^{-1} + \frac{V_{tc(384)}^{-1}}{\alpha_{(384)}} + \right. \right.$$

$$\left. \frac{V_{tc(221)}^{-1}}{\alpha_{(221)}} \right]^2 V_{\Delta Cm} + \left[\frac{V_{tc(384)}^{-1}}{\alpha_{(384)}} \right]^2 V_{\Delta Cb(384)} + \left[\frac{V_{tc(221)}^{-1}}{\alpha_{(221)}} \right]^2 V_{\Delta Cb(221)} \quad (12)$$

$$\left. + \left[\frac{\Delta C_m - \Delta C_{b(384)}}{\alpha_{(384)}^2 V_{tc(384)}} \right]^2 V_{\alpha(384)} + \left[\frac{\Delta C_m - \Delta C_{b(221)}}{\alpha_{(221)}^2 V_{tc(221)}} \right]^2 V_{\alpha(221)} \right),$$

from which the lifetime uncertainty was derived given Eq. (8). The PRD corresponding to the 384 keV and 221 keV γ-ray peaks was calculated using Eq. (5) to be $-80.6(31)$ ps, and the resulting lifetime calculations [12] are shown in Table 2.

For the geometry of this particular experiment, it is noted that the effect of the ToF correction is not significant as not only is the change in lifetime value smaller than the quoted uncertainty, the uncertainty itself has not been reduced after the correction was performed. Together with a comparison with the known lifetime data for ^{138}Gd, this observation is discussed in more detail in Section 5 by utilising Monte-Carlo simulations.

5. Discussion

The primary goal of the present work was to validate the fast-timing method with spatially distributed nuclei at the focal plane of a separator. The 2^+ state in ^{138}Gd was selected as a test case for this purpose as the lifetime was known [35]. The ToF correction due to the spatial distribution of recoils at the relatively small focal plane of the RITU spectrometer was found to have only a small effect on the measured lifetime. This situation is further assessed using Monte-Carlo simulations in the following sections together with a comparison between the present and available data. Using simulations, it is also shown that the ToF correction described in the present work will significantly reduce the uncertainties in the measured lifetimes for larger setups such as those at the focal plane of the Super-FRS at FAIR [56,57].

5.1. Comparison with previous measurements

The lifetime of the 2^+ state in ^{138}Gd was measured to be 308(17) ps in Ref. [35] using the RDM and two-fold γ-ray coincidence data which avoids the effect of side-feeding. This value is in agreement with 305(30) ps from an earlier measurement [58]. The ToF-corrected result of 229(24) ps from the present work is consistent with both published lifetime values within three standard deviations.

The present result for ^{138}Gd has a higher uncertainty than that obtained from measurements using the RDM. This can be attributed to the poor full-energy peak to background ratio seen in the γ-ray energy spectra (cf. Fig. 8). Therefore, more statistics and future fast-timing measurements with an incorporation of Compton suppression for LaBr$_3$ detectors could help to make reliable comparisons between the results obtained from the two methods. It is noted that the standard deviation of the spectra shown in Figs. 9(a) and (b) correspond to a timing resolution of 380 ps. This is larger than the measured value of $\sim$240 ps for similar γ ray energies corresponding to a ^{152}Eu source (cf. Section 3.1). This increase in standard deviation is likely due to the larger background contribution present in the in-beam data. In the following section, simulations were used to understand the observed precision in these results and the effect of the ToF corrections.

5.2. Monte-Carlo simulations

Monte-Carlo simulations were performed for a generalised experimental configuration and were applied to understand the results obtained in the present work using the specific detector geometry. The relevant details are presented in the following subsections. The influence of spatial distribution of the implanted recoils on the observed resolutions of the LaBr$_3$-time spectra, and thus on the achievable precisions of lifetime measurements, are particularly discussed. The effects of γ-ray background during the measurement and the PRD are not considered in these simulations.
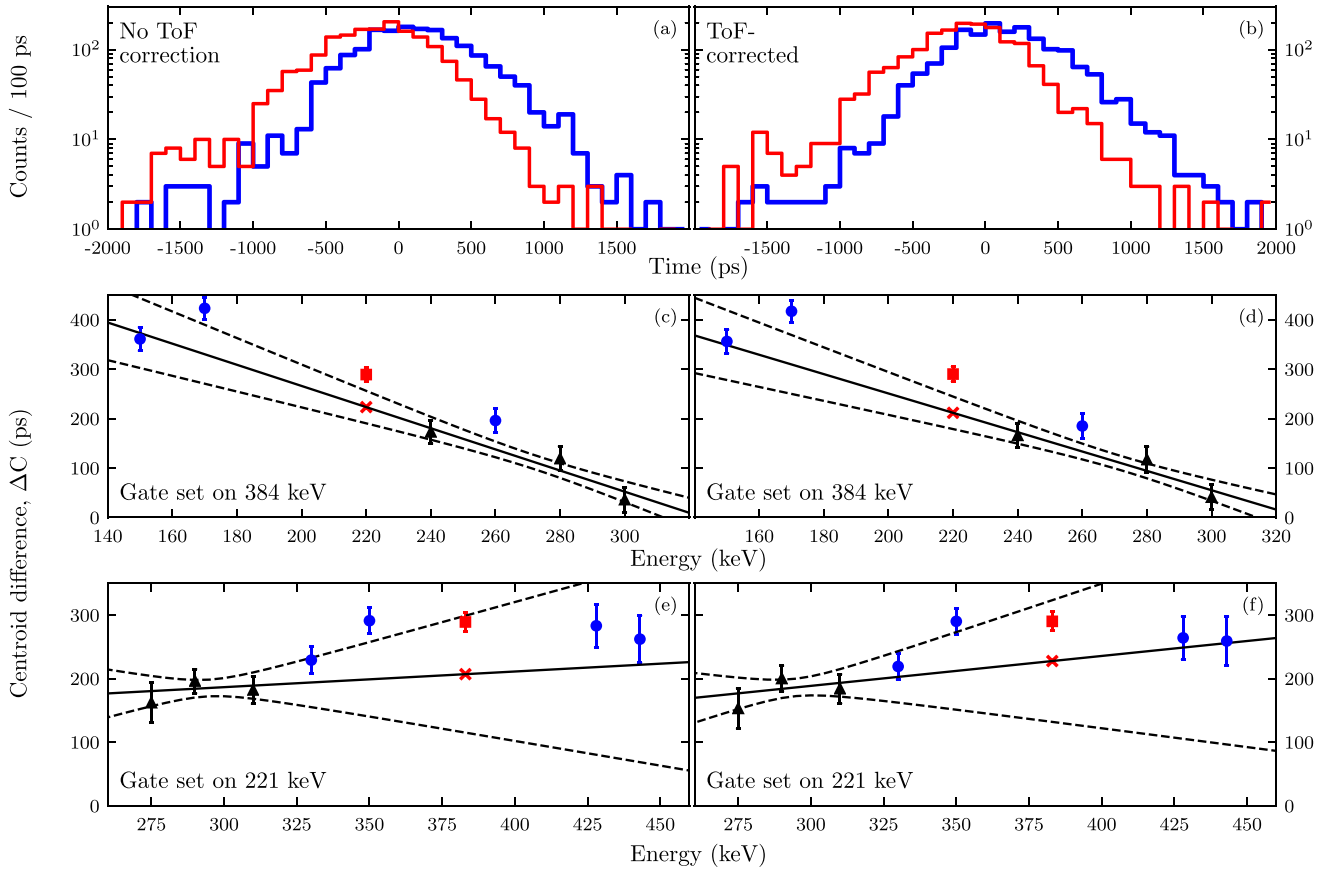
5.2.1. The influence of the spatial distribution of nuclei on timing resolution

For any given experimental setup, both the extent of the spatial distribution of implanted recoils and the specific detector geometry affect the magnitude and significance of the ToF correction given by Eq. (1). A computer code was written to calculate the correction for an arbitrary experimental setup. A number of events, N_0, representing timing measurements for the coincident γ rays populating and depopulating the level of interest, were distributed uniformly across each of the γ-ray detector pairs in the LaBr$_3$ array. For each count in one of the pairs, a value, value$_0$, was calculated according to

$$\text{value}_0 = \sigma_{\text{res}} \, \text{rng.Gaus()} + \Delta t_{\text{pos}}, \quad (13)$$

and binned into a histogram. Here, σ_{res} is the timing resolution of a LaBr$_3$ detector pair in the array. The random number generator, rng,

Fig. 9. Time spectra for the γ rays populating and depopulating the 2^+ state in ^{138}Gd (i.e. for 384 keV and 221 keV γ rays, respectively) both with no ToF correction being applied to the data ((a), (c) and (e)) and with the ToF correction (see text) being applied ((b), (d), (f)). The blue lines in (a) and (b) correspond to the delayed time spectra whilst the red lines correspond to the anti-delayed time spectra. The centroid difference of these spectra is shown as (red) square data points in (c) through (f). The background centroid difference values are shown by (black) triangular data points as a function of energy around the 221 keV peak ((c) and (d)) and the 384 keV peak ((e) and (f)). The solid line shows the best fit to selected background values, whilst the dashed line shows the one-standard-deviation intervals. The (red) cross is used to indicate the interpolated background centroid difference. The circular (blue) data points show background values that were not used in the interpolation due to possible contamination from other full-energy peak events. (For interpretation of the references to colour in this figure legend, the reader is referred to the web version of this article.)
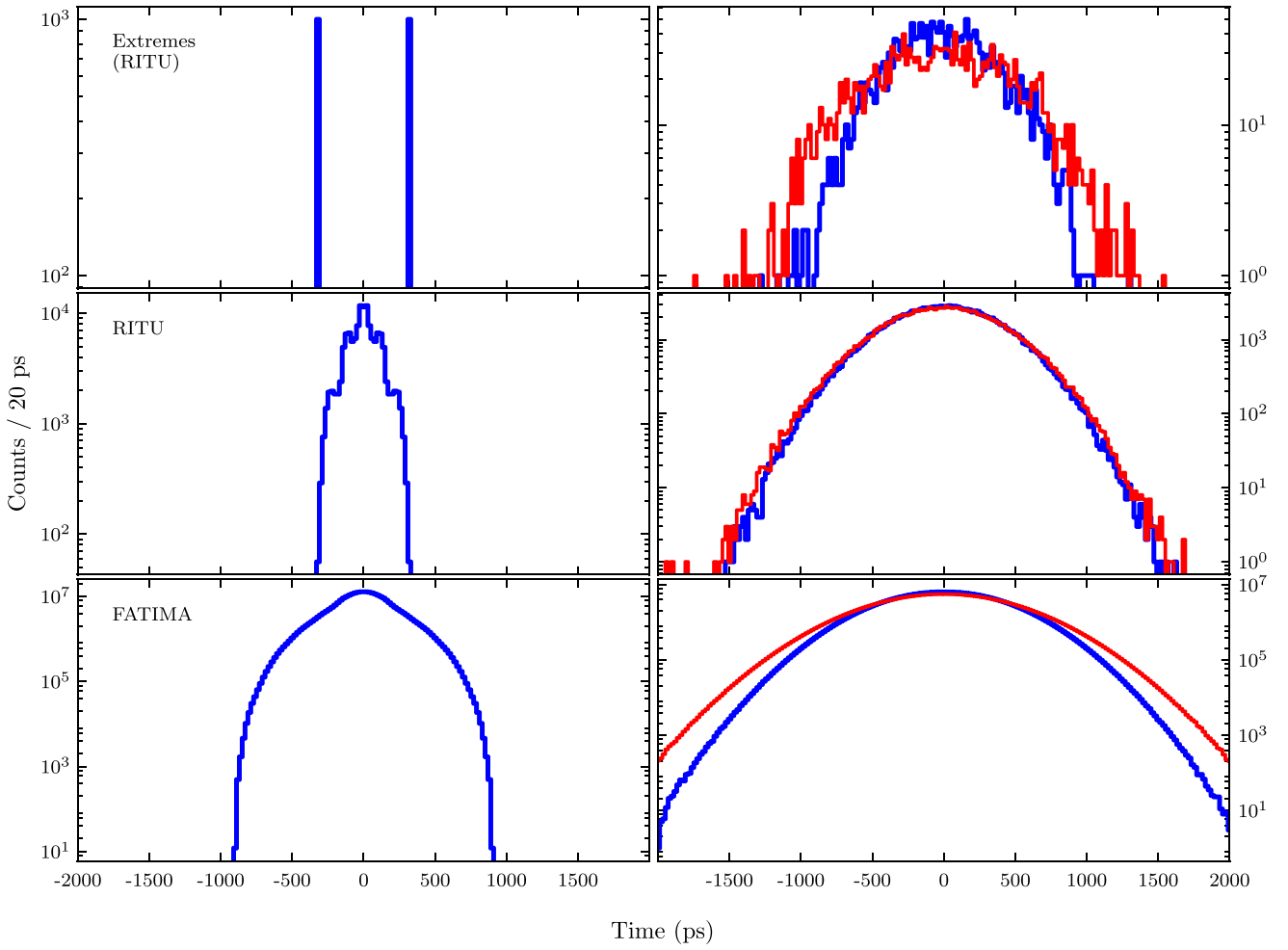
is provided by a python module [59] and is based on the Mersenne-Twister [60] algorithm. The function, rng.Gaus(), returned a random number following a Gaussian distribution with a mean of zero and a standard deviation of one. The maximum magnitude of Δt_{pos} across the DSSSD used in the present experiment was calculated to be ~330 ps. This corresponded to the DSSSD pixel with a recoil-implant closest to Detector 1 (top-left pixel of DSSSD as viewed when looking upstream of the recoil axis) acting as a source, with Detector 1 providing the start signal and Detector 8 providing the stop signal. With the source pixel in the opposite corner (bottom-right pixel of DSSSD), i.e. closest to Detector 8, the calculated ToF correction had equal magnitude and opposite sign. The difference between these two extreme positions was thus calculated to be ~660 ps. Fig. 10 (top-left) shows a histogram of values, value $_0$, calculated using Eq. (13) for $\sigma_{res} = 0$ for the two extreme pixels and detector pair (1, 8) under consideration. As expected, the separation in time between the peak centroids is ~660 ps. Fig. 10 (top-right) shows a histogram in red (blue) of value $_0$ with (without) Δt_{pos} in Eq. (13) and using $\sigma_{res} = 380$ ps from the present data. These representative time spectra demonstrate that the time resolution is worse if the ToF correction is not applied when considering the extreme positions.

Figs. 3–5 show that there were several different source positions across the area of the DSSSD and the 28 LaBr$_3$ detector-pair positions in the present experiment. Assuming an homogeneous distribution for implants across the DSSSD at the focal plane of RITU, histograms of calculated value $_0$ were prepared as shown in Fig. 10 (middle). The standard deviation of the time spectrum shown in Fig. 10 (middle-left), referred to as the distribution uncertainty, σ_{dist}, was found to be

~117 ps for RITU. The time spectra in blue and in red shown in Fig. 10 (middle-right) represent events with and without the ToF correction and have resolutions of 380 ps and 396 ps, respectively. It is worth noting that the observed non-homogeneous implantation distributions (cf. Fig. 3) result in a slightly different value of σ_{dist} ~110 ps. In this case, each of the calculated Δt_{pos} values for a given DSSSD pixel was weighted with the observed probability for recoil implantation in that pixel. In the present setup, the solid angle for different LaBr$_3$ detector-DSSSD-pixel combinations ranged between ~30 mSr and ~140 mSr. Therefore, the Δt_{pos} values should in principle be also weighted by the product of the corresponding solid-angle coverage of each detector in the pair. However, this consideration resulted in a small change of ~20 ps that is insignificant compared to the detector timing resolution of 380 ps. Fig. 10 (bottom) shows histogrammed Δt_{pos} values, which were calculated for the fast-timing detector geometry of the FATIMA setup, namely, a full array of 36 LaBr$_3$ detectors surrounding a stack of ten DSSSDs with a separation of 1 cm between any two of them in a 24 cm × 8 cm focal-plane configuration [56,57]. In this case, the distribution uncertainty was calculated to be $\sigma_{dist} = 220$ ps (Fig. 10 (bottom-left)), which is closer to the detector time resolution of 380 ps. Therefore, it is more important to apply the ToF correction to improve the time spectra. If uncorrected, a poorer resolution of ~440 ps will be observed (cf. Fig. 10 (bottom-right)).

5.2.2. The influence of distribution uncertainty on lifetime measurements

The results and discussions presented in the previous section demonstrate that a large spatial distribution of recoil-implants at the focal

Fig. 10. The histograms (left) show Δt_{pos}, highlighting the spread of the prompt time events due to the geometry of the LaBr$_3$ detectors and the DSSSD. The standard deviation of these spectra are referred to as the distribution uncertainty. The histograms on the right represent the time spectra with (blue) and without (red) the ToF correction having been applied. These were simulated by the calculation of σ_{res} rng.Gaus() and σ_{res} rng.Gaus() + Δt_{pos}, for the blue and red spectra, respectively. The top panels show the extreme time values from the present experiment, corresponding to the LaBr$_3$-detector-pair (1, 8) and pixels located in opposite corners of the DSSSD. The middle panels show Δt_{pos} as calculated for every combination of DSSSD pixel and LaBr$_3$-detector pair. The bottom panels show the Δt_{pos} calculation corresponding to an experimental setup of FATIMA. See the text for more details. (For interpretation of the references to colour in this figure legend, the reader is referred to the web version of this article.)

plane of a separator can potentially worsen the timing resolutions observed in fast-timing measurements. In the fast-timing technique, it is of importance to understand how the poorer resolution affects the uncertainty, σ_τ, in the measured lifetime, for example, using the GCD method. For this purpose, additional Monte-Carlo calculations were performed under the following assumptions; the prompt-response function followed a Gaussian distribution with a standard deviation of $\sigma_{res} = 380$ ps (based on the ^{138}Gd data), the lifetime to be measured was 230 ps (of similar order to the lifetime of the 2^+ state in ^{138}Gd as measured in the present work) and the alignment of the prompt-points of the 28 detector-pair components was assumed to have no error. This latter assumption is based on the observation that the 28 prompt-time points could be synchronised within $\sim$1 ps in the present work. Additional contribution to the lifetime uncertainty exists due to the prompt response difference correction, which was $\sim$3 ps in the present work (cf. PRD in Section 4). This error depends on the experimental setup and statistics in the source data and therefore needs to be optimised for a given setup. Lastly, background events, such as from Compton scatter, are completely ignored in these simulations. This ideal case results in the best-possible expected values, i.e. if there is no improvement observed in these simulations, there will almost certainly be no improvement in a measurement subject to background events.

A number of counts, N, were assumed to be distributed uniformly across each of the 28 detector pairs. For each count, a value was calculated according to

$$\text{value} = \sigma_{res}\ \text{rng.Gaus()} + \sigma_{dist}\ \text{rng.Gaus()} + \tau\ \text{rng.Exp()}, \qquad (14)$$

and binned into a histogram. Here, the function, rng.Exp(), returned a number following an exponential distribution with a characteristic lifetime of one. Therefore, the value was calculated by convoluting two Gaussian functions and an exponential with a prompt-point at 0 ps.

After all N values had been produced, the 28 resultant histograms were summed to produce the delayed-decay distribution, or delayed time spectrum. This was repeated, with a τ of equal magnitude and opposite sign, to form the anti-delayed [12] time spectrum that represents the reversing of the start and stop conditions in a TAC. Fig. 11 shows both the delayed and anti-delayed distributions for $N = 1000$. A value of $\sigma_{dist} = 110$ ps (cf. Section 5.2.1), calculated for the recoil implantation distribution shown in Fig. 3, was used in these simulations. The lifetime was subsequently calculated from the distributions shown in Fig. 11 using the GCD method [12]. This process was repeated 100 000 times, and a histogram of the resultant lifetimes is shown in Fig. 12. This histogram has a standard deviation of 10.239(23) ps, which is representative of the uncertainty of any given lifetime measurement. This is also close to the uncertainty of $\sim$11 ps in the fitted lifetime of 228(11) ps shown in Fig. 11.

The predicted uncertainty in the measured lifetime as a function of σ_{dist} is shown in Fig. 13. Each of these data points simulated using $N =$
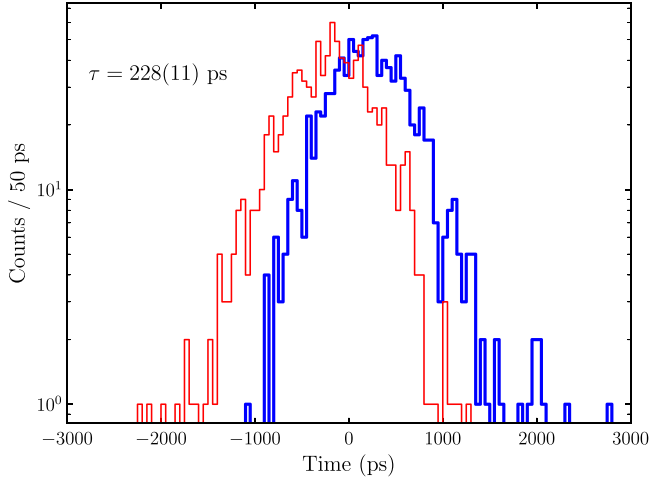
Fig. 11. Simulated spectra showing the delayed (blue) and anti-delayed (red) timing data, using $N = 1000$ and $\sigma_{dist} = 110$ ps. The value of $\tau = 228(11)$ ps was calculated from this data according to the GCD method. (For interpretation of the references to colour in this figure legend, the reader is referred to the web version of this article.)
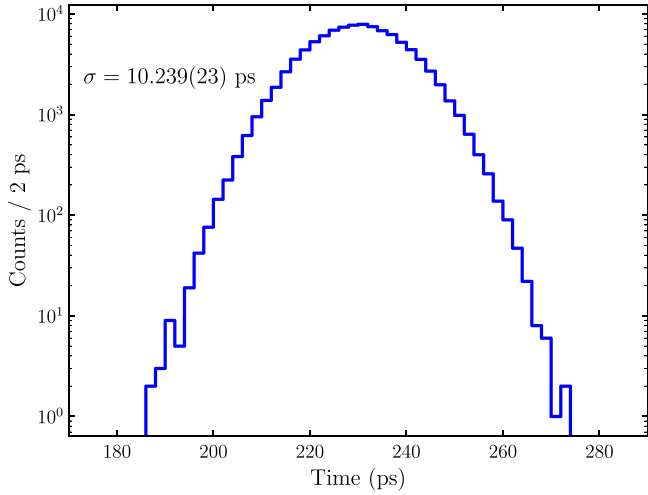

Fig. 12. A histogram of lifetimes obtained from 100 000 simulations such as the one shown in Fig. 11 for $N = 1000$, $\sigma_{dist} = 110$ ps. The standard deviation, σ, of the distribution gives the expected lifetime uncertainty from a single experiment.
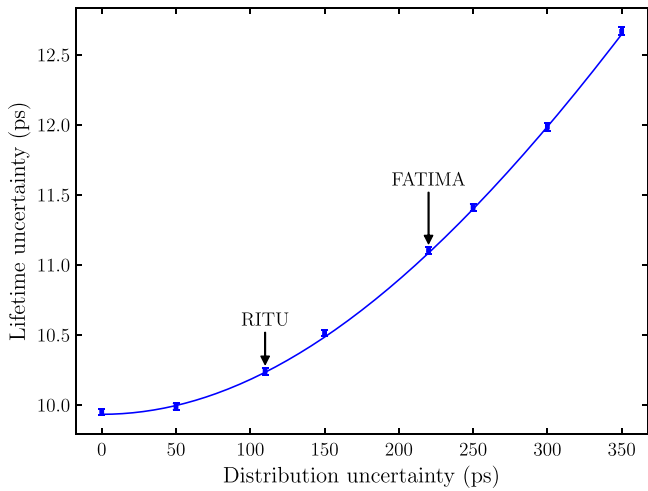

Fig. 13. The evolution of lifetime uncertainty, σ_τ, as a function of distribution uncertainty, σ_{dist}, for $N = 1000$ and $\tau = 230$ ps. The points corresponding to RITU and FATIMA are marked.

1000 for the underlying time spectra, close to the statistics observed in the data for ^{138}Gd. Different values of N, σ_{res} and τ were also tested and the uncertainty in the lifetime was found to be well described by

$$\sigma_\tau = \sqrt{\frac{\sigma_{res}^2 + \tau^2 + \sigma_{dist}^2}{2N}}. \tag{15}$$

Eq. (15) was derived by propagating the uncertainties of the convoluted spectra shown in Fig. 11, which each have a variance defined by the sum of the variances of the component distributions (i.e. $\sigma_{res}^2 + \tau^2 + \sigma_{dist}^2$) [61]. The point labelled as RITU in Fig. 13 with $\sigma_{dist} = 110$ ps corresponds to the present work on ^{138}Gd. It shows that $\sigma_\tau = 10.24$ ps would decrease by 3 % to 9.95 ps (i.e. the value at $\sigma_{dist} = 0$ ps) when the data were corrected for the ToF differences. This improvement is not significant, and therefore supports the result from Fig. 9 and Section 4 that the ToF correction procedure did not significantly improve the precision of measured lifetimes in the present work. In this particular case, the observed uncertainties were larger, i.e. the measured $\tau = 229(24)$ ps (cf. Table 2) for the 2^+ state in ^{138}Gd has more than double the uncertainty compared to that calculated from simulations ($\sim$10 ps). This difference between measurement and simulation mainly arises from the inclusion of background events (e.g. from Compton scatter) observed in the γ-ray energy spectra (cf. Fig. 8) and the propagated error due to the background-correction procedure.

6. Future experiments

6.1. Fast-timing measurements at facilities with larger focal plane areas

Experiments will be carried out in the future at larger separator focal planes such as that of the Super-FRS at the Facility for Antiproton and Ion Research (FAIR) [62]. Therefore, knowledge of the effect of spatial distribution of nuclei at such focal planes on σ_τ will be essential. In particular, recoil-implantation patterns such as those shown in Fig. 3 can significantly differ between different types of nuclear species with very large spatial distributions. Therefore, it will become increasingly important to apply the ToF corrections to lifetime data. For example, a value of $\sigma_{dist} = 220$ ps was calculated for the FATIMA fast-timing setup [56,57]. If no ToF correction is performed then an increase of $\sim$12 % in σ_τ can be estimated utilising the point labelled as FATIMA in Fig. 13.

6.2. Fast-timing measurements in exotic nuclei

The systematic errors in the measurements performed using the FTM and the RDM are independent and as such the two techniques complement each other. Nevertheless, the FTM has some advantages. Firstly, it can be employed both for the online (prompt or delayed) γ-ray data and for the offline γ-ray activity data as discussed in Section 1. Secondly, measurements can be performed by collecting data with lower statistics compared to that from the RDM. Therefore, the FTM might well be preferable over the RDM to study exotic nuclei at the limits of existence with low production cross sections. This can be illustrated through the previous RDM and the present FTM works on ^{138}Gd. Over the five-day experiment in the present work, $\sim$1000 counts were observed in the final TAC spectra for ^{138}Gd that is estimated to have a production cross section of 70 mb [63] and an isomeric yield of $\sim$1.4 % [19]. This resulted in an error of $\sim$25 ps for the measured lifetime, arising from statistics, the PRD uncertainty and the uncertainty of the background timing correction. The measurement using the RDM [35] was carried out for approximately 5 days using the same reaction and resulted in a comparable uncertainty on the lifetime measurement of 17 ps. Therefore, a $\sim$10 % uncertainty on the lifetime measurement can be expected from a fast-timing experiment with similar conditions and statistics. In the cases where the isomeric yields are higher than that in the present work, the accuracies can be further improved. For example, statistics would be doubled if the

isomeric ratio were 3 %, resulting in a ~7 % uncertainty on the lifetime. However, if higher-energy γ rays were to be considered, the timing resolution would be improved and the ToF correction becomes increasingly more important (cf. Eq. (15)). The same is true for the measurement of shorter nuclear-state lifetimes, where the distribution uncertainty begins to dominate the overall variance of the convoluted time spectra. For example, using the 130 ps resolution obtained for the ^{60}Co data (i.e. for ~1 MeV γ rays) presented in Fig. 2 and a lifetime of 100 ps, the lifetime uncertainty would increase by 20 % in the case of the present experimental setup at RITU. The equivalent increase in lifetime uncertainty for the FATIMA setup would be 67 % if the ToF correction was not performed. Further improvement can be expected from an incorporation of Compton suppression to improve full-energy peak to Compton-background ratio in the γ-ray spectra collected with LaBr$_3$ detectors.

7. Conclusion

In summary, a time-of-flight correction method for γ rays emitted from nuclei with large spatial distributions has been proposed and applied to fast-timing data. In addition, a new procedure to calibrate the time walk has been introduced that transparently deals with noted correlation issues. An array of eight LaBr$_3$ fast-timing detectors was used to detect the γ rays from recoils of interest implanted across a DSSSD with an area of 120 mm × 40 mm. An implanted-recoil position in the DSSSD was determined by measuring the energy deposition in a pixel and confirming that it corresponds to the expected energy of the recoils. This position information was then used to calculate the time-of-flight, corresponding to the path length travelled by each of the γ rays before being detected by a LaBr$_3$ detector. The ToF corrections to the fast-timing γ-ray data could thus be performed on an event-by-event basis. The effect of these ToF corrections on the uncertainties in the measured lifetimes were evaluated by comparing the results obtained using data with and without the corrections. For the detector geometry used and the spatial distribution of the implanted-recoils observed in the present work at the relatively small focal plane of RITU, this effect was found to be marginal. To understand this result, Monte-Carlo calculations were performed and the calculated path lengths for photons between the implantation positions and the LaBr$_3$ detectors resulted in an additional geometry dependent timing uncertainty (or the distribution uncertainty) of ~110 ps. A convolution of this uncertainty increased the value of the effective timing resolution of the eight LaBr$_3$ array from ~380 ps to ~396 ps for the low-energy (<500 keV) γ rays observed in the present work. Simulations showed that such an increase of ~4 % in timing resolution would result in a ~3 % larger uncertainty in the measured lifetime. The reason for only a marginal improvement in the time resolution upon the ToF correction in the present work is thus understood. Further simulations showed that the ToF correction is more significant for higher-energy γ rays, i.e. with better timing resolution, and for smaller lifetimes being measured. It is also shown that the lifetime measurements using recoil-implants with larger spatial distributions, which are expected in some of the future setups for exotic nuclei, will significantly benefit from the proposed ToF correction method.

Acknowledgements

References

[1] E. Sahin, et al., Phys. Rev. C 91 (2015) 034302.
[2] R. Julin, et al., J. Phys. G 43 (2016) 024004.
[3] F.M. Prados Estévez, et al., Phys. Rev. C 75 (2007) 014309.
[4] D. Ni, Z. Ren, Phys. Rev. C 82 (2010) 024311.
[5] T. Grahn, et al., Nuclear Phys. A 801 (2008) 83.
[6] M.G. Procter, et al., Phys. Lett. B 704 (2011) 118.
[7] M.G. Procter, et al., Phys. Lett. B 725 (2013) 79.
[8] D. Hodge, et al., Phys. Rev. C 94 (2016) 034321.
[9] D.S. Delion, et al., Phys. Rev. C 82 (2010) 024307.
[10] M.G. Procter, et al., Phys. Rev. C 86 (2012) 034308.
[11] P.J. Nolan, J.F. Sharpey-Schafer, Rep. Progr. Phys. 42 (1979) 1.
[12] J.-M. Régis, et al., Nucl. Instrum. Methods Phys. Res. A 726 (2013) 191.
[13] A. Dewald, O. Möller, P. Petkov, Nuclear Phys. 67 (2012) 786.
[14] D. Branford, I.F. Wright, Nucl. Instrum. Methods Phys. Res. 106 (1973) 437.
[15] T. Grahn, et al., Phys. Rev. Lett. 97 (2006) 062501.
[16] M. Doncel, et al., Phys. Rev. C 91 (2015) 061304.
[17] D. Bucurescu, et al., Nucl. Instrum. Methods Phys. Res. 837 (2016) 1, and the references therein.
[18] P.J.R. Mason, et al., Phys. Lett. B 683 (2010) 17.
[19] D.M. Cullen, et al., Phys. Rev. C 58 (1998) 846.
[20] C. Scholey, et al., Phys. Rev. C 63 (2001) 034321.
[21] D.M. Cullen, et al., Phys. Rev. C 66 (2002) 034308.
[22] P.J.R. Mason, et al., Phys. Rev. C 79 (2009) 024318.
[23] D.M. Cullen, et al., Phys. Rev. C 80 (2009) 024303.
[24] P.J.R. Mason, et al., Phys. Rev. C 81 (2010) 024302.
[25] M.G. Procter, et al., Phys. Rev. C 83 (2011) 034311.
[26] D. Hodge, et al., Phys. Rev. C 92 (2015) 054312.
[27] P.J.R. Mason, et al., Phys. Rev. C 85 (2012) 064303.
[28] C.R. Niţă, et al., Phys. Rev. C 89 (2014) 064314.
[29] C.W. Beausang, et al., Nucl. Instrum. Methods Phys. Res. A 313 (1992) 37.
[30] G. Duchêne, et al., Nucl. Instrum. Methods Phys. Res. A 432 (1999) 90.
[31] C.W. Beausang, J. Simpson, J. Phys. G 22 (1996) 527.
[32] M. Leino, et al., Nucl. Instrum. Methods Phys. Res. B 99 (1995) 653.
[33] R.D. Page, et al., Nucl. Instrum. Methods Phys. Res. B 204 (2003) 634.
[34] M. Labiche, private communication.
[35] M.G. Procter, et al., Phys. Rev. C 84 (2011) 024314.
[36] Hamamatsu, Photomultiplier tube R9779. http://www.hamamatsu.su/pdf/etd/R9779_TPMH1297E06.pdf.
[37] ORTEC, Model 474 Timing Filter Amplifier Operating and Service Manual. www.ortec-online.com/download/474-MNL.pdf.
[38] ORTEC, Model 935 Quad Constant-Fraction 200-Mhz Discriminator Operating and Service Manual. www.ortec-online.com/download/935-MNL.pdf.
[39] ORTEC, Model 566 Time-to-Amplitude Converter (TAC) Operating and Service Manual. www.ortec-online.com/download/566-MNL.pdf.
[40] I. Lazarus, et al., IEEE Trans. Nucl. Sci. 48 (2001) 567.
[41] P. Rahkila, Nucl. Instrum. Methods Phys. Res. A 595 (2008) 637.
[42] D.C. Radford, Nucl. Instrum. Methods Phys. Res. A 361 (1995) 297.
[43] J.P. Terlouw, M.G.R. Vogelaar, Kapteyn Package, version 2.3, Kapteyn Astronomical Institute, Groningen, 2015.
[44] K. Levenberg, Quart. App. Maths. 2 (1944) 164.
[45] D.W. Marquardt, J. Soc. Ind. App. Maths. 11 (1963) 431.
[46] J.-M. Régis, et al., Nucl. Instrum. Methods Phys. Res. A 684 (2012) 36.
[47] T.J. Paulus, IEEE Trans. Nucl. Sci. 32 (1985) 1242.
[48] J.K. Tuli, Nucl. Data Sheets 100 (2003) 347.
[49] ORTEC, Fast-timing discriminator introduction. http://www.ortec-online.com/download/fast-timing-discriminator-introduction.pdf.
[50] M.J. Martin, Nucl. Data Sheets 114 (2013) 1497.
[51] J.-M. Régis, G. Pascovici, J. Jolie, M. Rudigier, Nucl. Instrum. Methods Phys. Res. A 622 (2010) 83.
[52] E.O. Lebigot, Uncertainties: a Python package for calculations with uncertainties. http://pythonhosted.org/uncertainties/.
[53] J. Chen, Nucl. Data Sheets 146 (2017) 252–323.
[54] F. Soramel, et al., Phys. Rev. C 38 (1988) 537.
[55] S. Ansari, et al., Phys. Rev. C 96 (2017) 054323.
[56] Zs. Podolyák, Radiat. Phys. Chem. 95 (2014) 14.
[57] P.H. Regan, Radiat. Phys. Chem. 116 (2015) 38.
[58] P.J. Bishop, et al., J. Phys. G 14 (1988) 995.
[59] S. van der Walt, S.C. Colbert, G. Varoquaux, Comput. Sci. Eng. 13 (2011) 22.
[60] M. Matsumoto, T. Nishimura, ACM Trans. Model. Comput. Simul. 8 (1998) 3.
[61] C.A. Laury-Micoulaut, Astron. Astrophys. 51 (1976) 343.
[62] O.J. Roberts, et al., Nucl. Instrum. Methods Phys. Res. A 748 (2014) 91.
[63] A. Gavron, Phys. Rev. C 21 (1980) 230.